2-27-2014

WRF summer extreme daily precipitation over the CORDEX Arctic

Justin M. Glisan
Iowa State University, glisanj@iastate.edu

William J. Gutowski Jr.
Iowa State University, gutowski@iastate.edu

WRF summer extreme daily precipitation over the CORDEX Arctic

Abstract
We analyze daily precipitation extremes produced by a six-member ensemble of the Pan-Arctic Weather Research and Forecasting (WRF) that simulated 19 years on the Coordinated Regional Climate Downscaling Experiment (CORDEX) Arctic domain for the Arctic summer. Attention focuses on four North American analysis regions defined using climatological records, regional weather patterns, and geographical/topographical features. We compare simulated extremes with those occurring at corresponding observing stations in the U.S. National Climate Data Center's Global Summary of the Day. Our analysis focuses on variations in features of the extremes such as magnitudes, spatial scales, and temporal regimes between regions. Using composites of extreme events, we also analyze the processes producing these extremes, comparing circulation, pressure, temperature, and humidity fields from the ERA-Interim reanalysis and the model output. Although the model's extreme precipitation is low compared to the observed one, the physical behavior in the reanalysis leading to observed extremes is simulated in the model. In particular, the reanalysis and the model both show the importance of moisture advection against topography for producing most of the extreme daily precipitation events in summer. In contrast, parts of Arctic western Canada also have a substantial contribution from convective precipitation, which is not seen in the other regions analyzed. The analysis establishes the physical credibility of the simulations for extreme behavior. It also highlights the utility of the model for extracting behaviors that are not easily discernible from the observations such as convective precipitation.

Keywords
Precipitation extremes, Regional climate modeling, North American Arctic, Convection, Topographical forcing

Disciplines
Climate

Comments
This article is from *Journal of Geophysical Research: Atmospheres* 119 (2014): 1720–1732, doi:10.1002/2013JD020697. Posted with permission.

AGU PUBLICATIONS

JGR

Journal of Geophysical Research: Atmospheres

RESEARCH ARTICLE
10.1002/2013JD020697

Key Points:
- Simulations give insight into the nature of extremes in select Arctic regions
- Establishes the physical credibility of WRF simulations for extreme behavior
- Impact of topography on creating widespread precipitation extremes

Correspondence to:
J. M. Glisan,
glisanj@iastate.edu

Citation:
Glisan, J. M., and W. J. Gutowski Jr. (2014), WRF summer extreme daily precipitation over the CORDEX Arctic, *J. Geophys. Res. Atmos.*, *119*, 1720–1732, doi:10.1002/2013JD020697.

Received 8 AUG 2013
Accepted 22 JAN 2014
Accepted article online 27 JAN 2014
Published online 25 FEB 2014

WRF summer extreme daily precipitation over the CORDEX Arctic

Justin M. Glisan[1] and William J. Gutowski Jr.[1]

[1]Department of Geological and Atmospheric Sciences, Iowa State University of Science and Technology, Ames, Iowa, USA

Abstract We analyze daily precipitation extremes produced by a six-member ensemble of the Pan-Arctic Weather Research and Forecasting (WRF) that simulated 19 years on the Coordinated Regional Climate Downscaling Experiment (CORDEX) Arctic domain for the Arctic summer. Attention focuses on four North American analysis regions defined using climatological records, regional weather patterns, and geographical/topographical features. We compare simulated extremes with those occurring at corresponding observing stations in the U.S. National Climate Data Center's Global Summary of the Day. Our analysis focuses on variations in features of the extremes such as magnitudes, spatial scales, and temporal regimes between regions. Using composites of extreme events, we also analyze the processes producing these extremes, comparing circulation, pressure, temperature, and humidity fields from the ERA-Interim reanalysis and the model output. Although the model's extreme precipitation is low compared to the observed one, the physical behavior in the reanalysis leading to observed extremes is simulated in the model. In particular, the reanalysis and the model both show the importance of moisture advection against topography for producing most of the extreme daily precipitation events in summer. In contrast, parts of Arctic western Canada also have a substantial contribution from convective precipitation, which is not seen in the other regions analyzed. The analysis establishes the physical credibility of the simulations for extreme behavior. It also highlights the utility of the model for extracting behaviors that are not easily discernible from the observations such as convective precipitation.

1. Introduction

Extreme precipitation events can affect both anthropogenic and natural systems. If these events are spatially widespread, both systems can experience substantial impacts, such as flooding and land erosion. Runoff from land-based extreme precipitation events also contributes to the Arctic Ocean's relatively fresh surface waters [*Barry and Serreze*, 2000], which strongly influence growth and maintenance of sea ice [*Cassano et al*., 2007]. The Arctic is experiencing substantial climate change [*Serreze et al*., 2009] and is projected to experience greater change in the future than most of the planet [*IPCC*, 2007; *Ghatak and Miller*, 2013]. This enhanced, high-latitude warming motivates a need to understand how climate change will affect extremes and their expected increase in occurrence [*Tebaldi et al*., 2006].

With increased warming in the Arctic, model studies indicate that extreme precipitation events will also increase, including over North America [*Kunkel*, 2003]. For example, *Zhang et al*. [2001] show that North American extremes usually occurring every 20 years in contemporary climate are projected to occur in half that time in a warmer climate. Canada would also undergo an average increase in extreme precipitation events of 14% when compared to the last decade of the twentieth century. *Schindler and Smol* [2006] show spatially widespread precipitation events increase freshwater runoff into the Arctic Basin and exacerbate surface flooding. Thus, extreme events are likely to have an increasingly strong impact on human and natural processes as the Arctic warms.

Establishing the capability of regional climate models (RCMs) to produce precipitation events well is important. Global climate models (GCMs) with typical resolutions over polar land areas of 150–200 km may lack sufficient resolution to capture precipitation extremes and, equally important, their causal processes. At these resolutions, Arctic processes such as surface-based physical responses to sea ice and snow cover and the highly stable polar inversion are difficult to simulate [*Dethloff et al*., 1996]. Development of Arctic-focused RCMs is thus an important step in understanding polar extremes and their underlying processes [*Matthes et al*., 2010]. Here we examine the ability of a polar-optimized RCM to produce observationally consistent

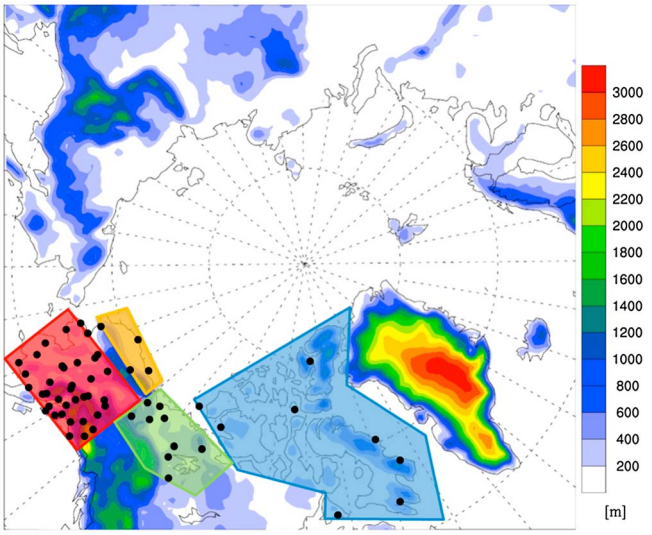

Figure 1. CORDEX Arctic 50 km domain with the North American analysis regions. Individual analysis regions denoted by colored boxes. Coloring on the land portions of the plot represents topography height. Black dots represent NCDC stations.

mean and daily extreme precipitation. We also evaluate the ability of the model to produce the physical processes responsible for extreme precipitation.

Simulations with 50 km resolution can give an adequate representation of daily precipitation extremes in regions of rapidly varying topography [*Gutowski et al*., 2007]. Thus, finer grid spacing than is typical in current GCMs may give a better rendition of physical mechanisms responsible for daily extreme precipitation events in the Arctic. In turn, RCMs that can produce real world physical processes responsible for extremes are then an important tool in the evaluation of potential future changes in extreme precipitation.

Our simulations use the Arctic domain developed for the Coordinated Regional Climate Downscaling Experiment (CORDEX) [*Giorgi et al*., 2009], and our diagnosis focuses on four Arctic analysis regions. We concentrate on land-based extreme daily precipitation events occurring in the summer from 1992 through 2007. The paper is organized as follows: Section 2 describes the Pan-Arctic WRF model and simulations. Section 3 details the evaluation methodology for analysis. Section 4 describes our results, and section 5 gives our conclusions.

2. Model and Simulations

2.1. Pan-Arctic WRF (PAW)

We used version 3.1.1 of the Weather Research and Forecasting—Advanced Research WRF [*Skamarock et al*., 2008]. Selection of Arctic-appropriate physical parameterizations was an important consideration for our model simulations. We used parameterization choices discussed in *Cassano et al*. [2011] with further modifications based on work by M. Seefeldt (unpublished data, 2010).

For water condensation, we used the subgrid cumulus scheme of *Grell and Devenyi* [2002] and the Goddard Cumulus Ensemble models microphysical scheme [*Tao and Simpson*, 1993] using three categories of ice phase. For the planetary boundary layer, we used the Mellor-Yamada-Janić scheme [*Janjić*, 1990, 1996, 2002], and for the surface layer, the Eta model [*Janjić*, 1996, 2002] which employs the Monin-Obukhov similarity theory [*Monin and Obukhov*, 1954]. Shortwave and longwave radiation used the National Center for Atmospheric Research Community Atmospheric Model spectral-band scheme [*Mlawer et al*., 1997; *Collins et al*., 2004]. A polar-specified land surface model (LSM) was also an important part of our simulations; we used the four-layer Noah LSM [*Chen and Dudhia*, 2001] as modified by *Hines et al*. [2011]. Guided by *Cassano et al*. [2011], we set the sea ice albedo and emissivity at 0.80 and 0.98, respectively.

2.2. Model Domain and Simulation

We used the Arctic domain specified by CORDEX. The domain (Figure 1) contains all of the Northern Hemisphere's sea ice cover and encompasses most of the Arctic drainage system. Moreover, it contains critical interocean exchange and transport circulations important for regional climate modeling. We used the standard CORDEX horizontal resolution of 50 km. The model used 40 unequally spaced sigma levels for vertical resolution, with the model top at 0.5 hPa and the lowest level at 12.5 m above ground level (agl).

2.3. Initial and Boundary Conditions

Initial and lateral boundary conditions for PAW used two distinct data sets. For initial conditions, simulations used the European Centre for Medium-Range Weather Forecasts ERA-Interim (EI) reanalysis [*Dee et al*., 2011].

The EI output is available on a reduced Gaussian grid with a uniform, approximately 79 km horizontal grid spacing and 60 vertical levels, up to 0.1 hPa. The EI fields are available every 6 h, starting from 1989 through 2007. Various studies of WRF simulation in the Arctic have shown that the EI performs better than other reanalysis products [*Cassano et al.*, 2011; *Glisan et al.*, 2013]. The model also used the Bootstrap Sea Ice Concentrations from Nimbus-7 scanning multichannel microwave radiometer and DMSP SSM/I satellite sensors [*Comiso*, 2008] archived at the U.S. National Snow and Ice Data Center. The native grid format for the ice concentration data is the SSM/I polar stereographic grid (25 × 25 km). Although WRF can use interior nudging as part of its external forcing, for the simulations here, we did not find it necessary and so there was no interior nudging.

2.4. Simulations

Our simulations produced a six-member PAW ensemble on the CORDEX-Arctic domain covering the period of 1989–2007. We determined that this ensemble size was appropriate to obtain the correct seasonal response from the model [*Taschetto and England*, 2008]. To produce the ensembles, we chose a 24 h staggered start between successive members. *Glisan et al.* [2013] showed that this method allows the ensemble to develop adequate ensemble spread due to the model's nonlinear internal variability. We discarded the first 3 years of the simulation since they were used to spin-up land surface processes.

We focus on the summer season, which is defined by the sea ice cycle. Specifically, we choose the months July, August, and September, the period leading to the minimum Arctic sea ice extent. In summer, smaller-scale (e.g., mesoscale) processes may be of greater significance than in winter for the production of precipitation events. These smaller-scale circulation dynamics may present some difficulties, as they can be subgrid scale even at our resolution.

3. Analysis Methods

3.1. Observational Data

Model validation compares the model output against two data sets. The EI reanalysis provides output for composite, observation-based fields and model bias analysis. We do not use EI precipitation because it is a model product that is not constrained by precipitation observations.

The second data set is the National Climate Data Center's (NCDC) Global Summary of the Day [*National Climate Data Center*, 2011], which provides both temperature and precipitation observations. Within the CORDEX-Arctic domain there are nearly 150 stations with available observations, some of which date back to the 1940s. While NCDC does perform quality control on the station data, to ensure data continuity, our analysis requires that an acceptable station have no more than four missing days in any month.

3.2. Analysis Regions

To analyze extreme precipitation and causal processes, we focused on two analysis regions in both Alaska and Canada (Figure 2). We used climatological records and regional weather patterns to help define these regions. The Aleutian Low and Beaufort High, which are semipermanent synoptic pressure features, have a particularly strong influence on precipitation processes across Alaska and western Canada. In terms of eastern Canada, the Icelandic Low is a dominant controlling pressure feature. We also found that the NCDC stations were located near higher-populated areas or airports and in geographical regions more conducive for station maintenance. These features aided us in producing the analysis regions because of "natural" breaks in stations across Alaska and Canada:

1. Canada East: The Canadian Archipelago—Stations within this box are located on islands making up the archipelago. Nearly a quarter of these stations are north of the Arctic Circle.
2. Canada West: East of the Canadian Rockies—Stations here are in the Canadian interior, spanning the sub-Arctic Canadian plains.
3. Alaska North: North of the Brooks Range, plus Arctic Sea stations—Stations here all reside north of the Arctic Circle and are thus highly influenced by the Arctic Ocean (including sea ice processes and the circumpolar vortex).
4. Alaska South: South of the Brooks Range and west of the Canadian Rockies—Stations here are influenced by the North Pacific storm track.

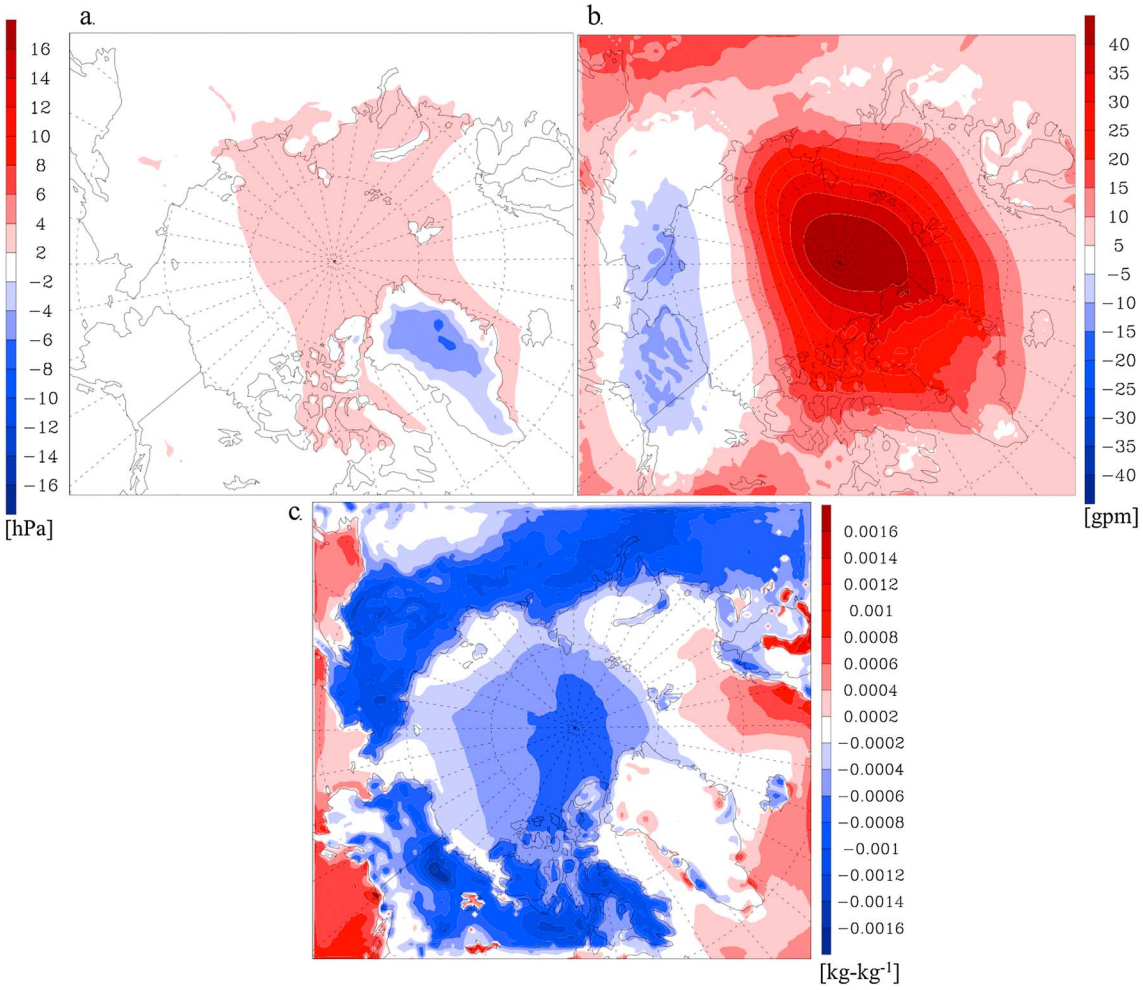

Figure 2. Pan-Arctic WRF-ERA Interim reanalysis 16 year JAS (a) mean sea level pressure bias (hPa), (b) 500 hPa geopotential height bias (geopotential meters), and (c) 2 m specific humidity bias (kg kg^{-1}).

3.3. Simulation Bias

To assess how well our simulations produced observationally consistent output, we used seasonal mean plots of PAW-EI bias for surface and various pressure-level fields. We analyzed the 16 year seasonal mean bias from the model and reanalysis for sea level pressure, surface and pressure level temperatures, surface specific humidity, and 500 hPa geopotential heights.

3.4. Precipitation Extremes

We extracted extreme precipitation events using procedures presented in *Gutowski et al.* [2007]. Daily events were defined as a single grid point or NCDC station having precipitation greater than 2.5 mm. We chose this threshold since the NCDC stations do not record precipitation below 2.5 mm. We pooled all events in an analysis region for further study.

We constructed two sets of plots to aid in our analysis of precipitation extremes. The first set was frequency versus precipitation histograms. We used the *Wilks* [1995] criterion to avoid excessively coarse or fine bin widths. We normalized the histograms by dividing each bin's count of events by the total number of events tallied from a data source. Using these diagrams, we defined extreme events as those occurring at the 99th percentile or higher. The second set of plots gave the number of extreme events occurring on at least *N* grid points simultaneously (i.e., on the same day). The simultaneity plots gave an indication of the spatial scale of extreme events. While each ensemble member had the same number of grid points, (and approximately the same number of events) the number of observation points (stations) was smaller than the number of grid points. Thus, we used a normalization procedure for the simultaneity plots to account approximately

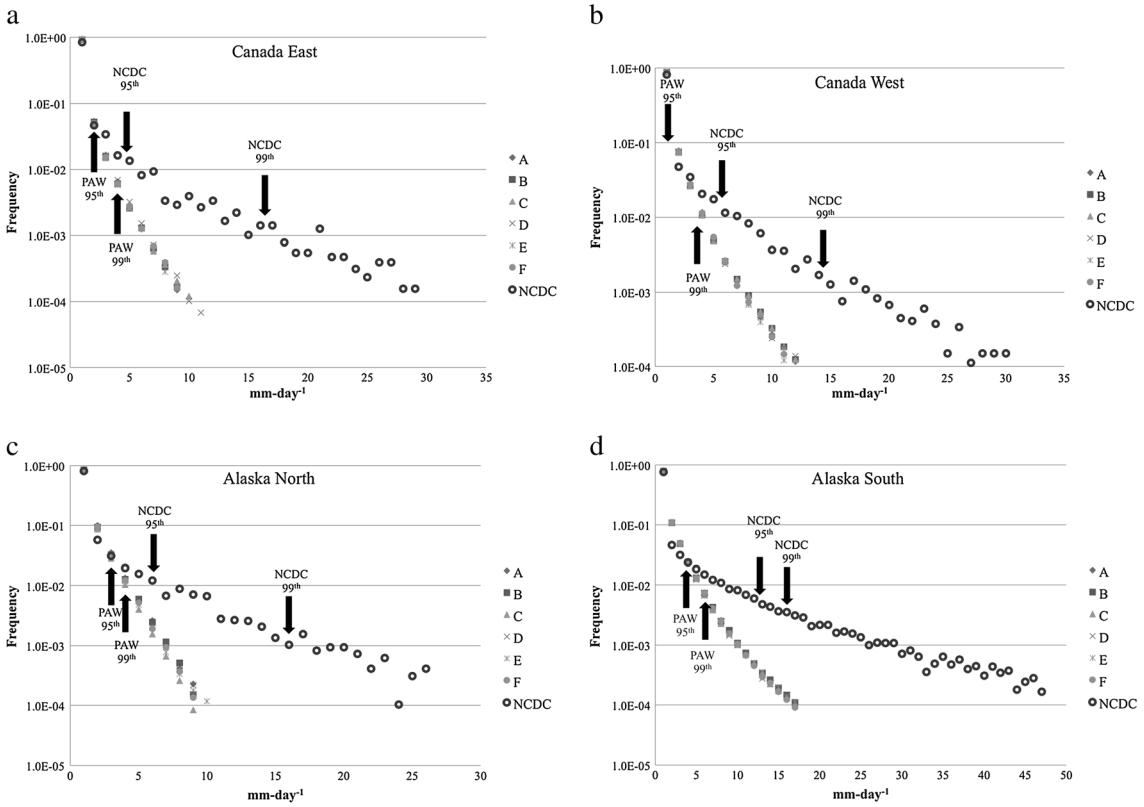

Figure 3. Frequency versus intensity distribution of Pan-Arctic WRF ensemble and NCDC station observations for (a) Canada East and (b) Canada West. Red (blue) arrows mark the 95th and 99th percentiles for PAW (NCDC). The simulation ensemble members are denoted A–F. Frequency versus intensity distribution of Pan-Arctic WRF ensemble and NCDC station observations for (c) Alaska North and (d) Alaska South. Red (blue) arrows mark the 95th and 99th percentiles for PAW (NCDC). The simulation ensemble members are denoted A–F.

for the differences in spatial resolution of the simulations and the observation stations. In each analysis region, we divided the total number of model grid points by the total number of NCDC stations. This value was then used to estimate the number of model grid points represented by an observation point. We use the simultaneity plots to define "widespread extremes," which here were daily extremes occurring simultaneously over 25 or more model grid points within an analysis region.

3.5. Circulation Diagnostics

To understand how well the PAW simulations produce observationally consistent behavior; we used seasonal mean bias plots of surface and upper level variables. These biases allowed us to discern better the areas within the domain that are more difficult to model.

We diagnosed the relevant circulation and related features of widespread extreme precipitation using fields of several diagnosed variables. Using the widespread extreme criterion, we extract the days with widespread extremes from the ensemble and composite their fields. We performed this procedure separately for each analysis region. For observational comparison, we used the same steps for the NCDC stations to extract widespread extremes in the observations. Once the relevant days were extracted, we used the EI reanalysis to produce composited fields, as the NCDC observations did not include upper air observations.

We also produced, for each analysis region, composite anomaly plots, calculated from the difference of our widespread extreme composites and the seasonal climatology. The anomalies showed how extreme events depart from mean atmospheric behavior.

Since portions of our analysis regions were within the midlatitudes, convective processes might have been present during the summer. To further understand the role of convection in the production of extreme precipitation events, we calculated the simulation's convective contribution to the total rainfall on widespread extreme days. With this information, we were able to determine which analysis regions were candidates for further convective analysis. This analysis included composite plots of various indices used to diagnose convective behavior.

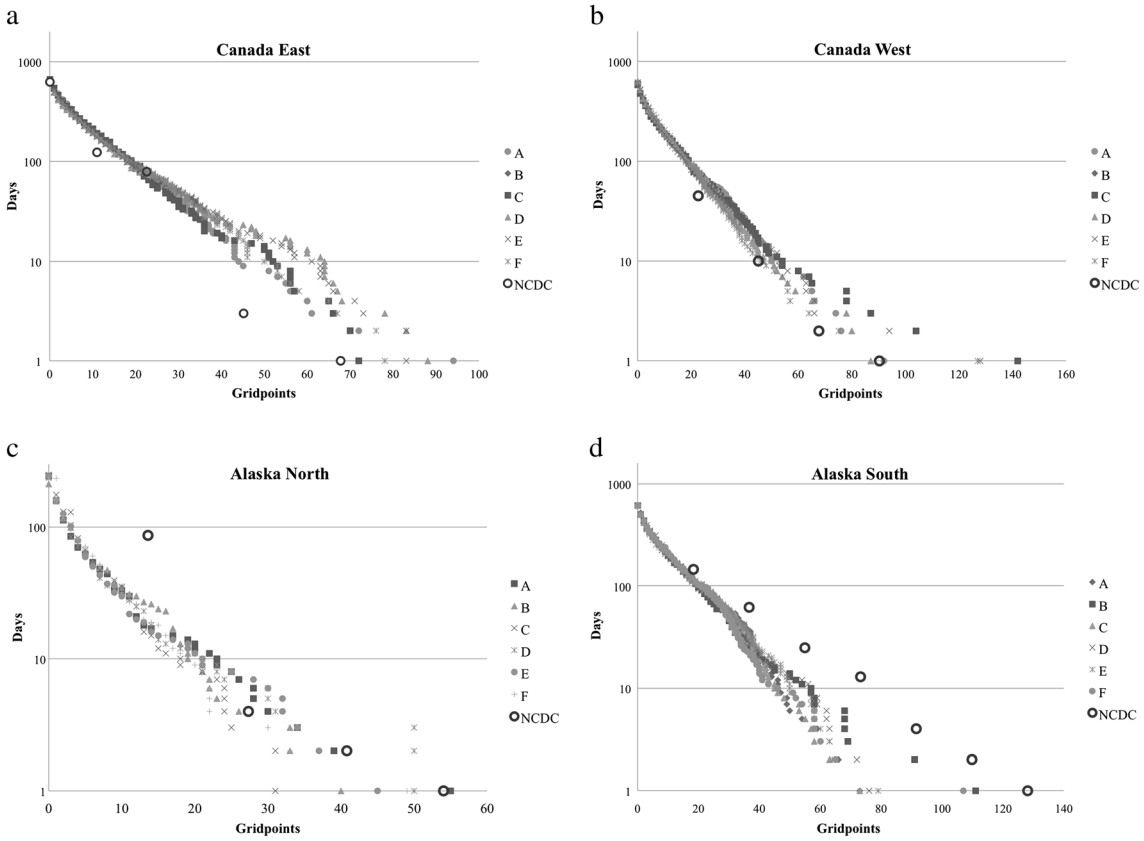

Figure 4. Number of days having at least *N* grid points with precipitation exceeding the 99th percentile in the Pan-Arctic WRF ensemble and NCDC station observations for (a) Canada East and (b) Canada West. The simulation ensemble members are denoted A–F.

4. Results

4.1. Spatial Climatology Bias

PAW-EI mean biases (Figures 2) show that simulated behavior agrees well with observations. The mean sea level pressure (MSLP) has its largest absolute bias over the high topography of Greenland (Figure 2a). The bias appears to result from differences between the reanalysis and the model in how each computes MSLP in regions of high topography. Otherwise, the magnitude of the bias is less than 4 hPa, which is relatively small compared daily variability [*Fisel et al.*, 2011]. Figure 2b shows differences in 500 hPa geopotential heights ranging from −10 to + 40 geopotential meters (gpm) with the positive height bias coincident with the positive MSLP bias. These differences are smaller than the daily variability of 500 hPa heights of about 100 gpm in the central Arctic [*Wei et al.*, 2002]. Near-surface atmospheric humidity bias has its largest values over land (Figure 2c). These results suggest PAW is systematically simulating drier conditions in the warm season. However, biases across the Arctic are much smaller than observed climatological humidity values of roughly 0.003 kg kg^{-1} [*Oort*, 1983; *Serreze et al.*, 1997]. Overall, biases are relatively small, especially in our analysis regions.

4.2. Precipitation Frequency Versus Intensity

Figure 3 shows daily precipitation's pooled 16 year frequency versus intensity for each analysis region. The model consistently underestimates extreme precipitation amounts. We find best agreement at the lower intensity end of the spectrum. The figure shows that the 95th and 99th percentile levels are substantially higher in the observations. We also note that there is not a substantial amount of spread between the ensemble members. For further work, we define extreme precipitation as daily amounts at the 99th percentile or higher, recognizing the difference between observed and simulated values.

Figure 4 shows the number of days having at least *N* grid points with precipitation exceeding the 99th percentile, for each analysis region. All ensemble members are plotted individually, with the NCDC observations

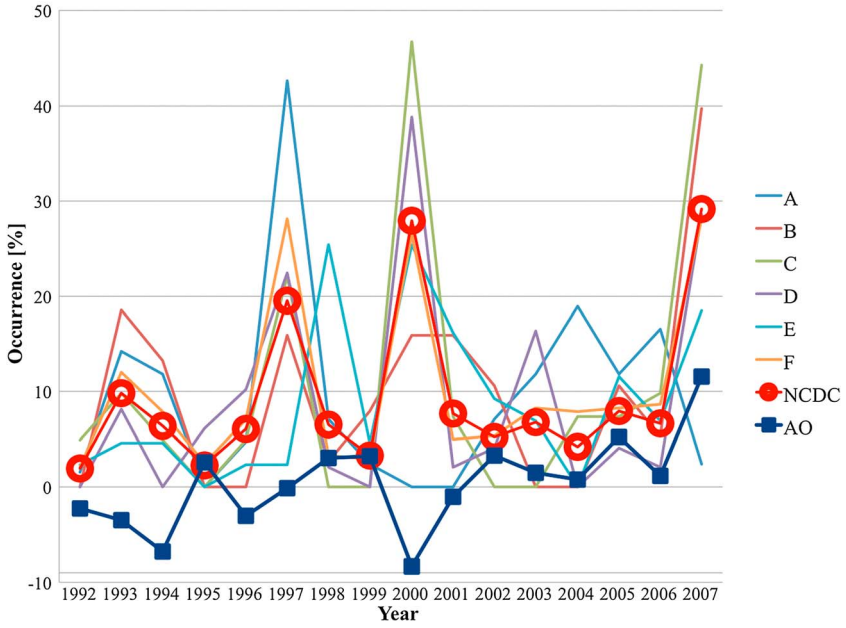

Figure 5. The interannual variability of daily widespread extreme precipitation occurrences (%) in the Alaska South analysis region. Pan-Arctic WRF ensemble members are plotted in smooth lines. NCDC observations are plotted in red, and the Arctic Oscillation (AO) Index is plotted in blue. The AO Index has been scaled by a factor of 5 in order to compare with PAW and NCDC.

scaled as discussed earlier. All analysis regions display nearly identical behavior. We define "widespread events" as those occurring simultaneously on 25 or more model grid points (or a comparable number of scaled observation points). This choice balances a goal of having a moderately large number of samples to analyze against an assumption that widespread extremes are governed by resolved fields in the simulations.

The curves for each of the ensemble members tend to group together for N up to about 50, for three of the regions. The Alaska North box shows greater spread among ensemble members, with separation of curves from individual members occurring at around $N = 10$ grid points. More importantly, the simulation curves show fair agreement with the observation curves; the slopes of the model and observation curves in Figure 4 differ by less than 10% on the log linear plot. This suggests that the spatial scale for simulated extreme events is roughly the same as the observed scale, despite the weaker precipitation extremes in the simulations.

4.3. Interannual Variability of Daily Precipitation Extremes

To understand the interannual variability of widespread precipitation events during the simulation period, we have plotted the percentage of extreme events occurring in each year for PAW ensemble members and NCDC observations. Figure 5 shows the Alaska South results as an example. The ensemble as a whole tends to follow the interannual variability of the NCDC observations, with noteworthy maxima in 1993, 1997, 2000, and 2007. The plots for the remaining analysis regions (not shown) show similar behavior.

Since our analysis regions are in the higher latitudes, we were also interested in whether or not the Arctic Oscillation (AO) had any control over interannual variability of the widespread extremes. The AO is a pattern of pressure fluctuations that affect the path of storm systems in the higher latitudes [*Thompson and Wallace*, 1998, 2001]. A positive (negative) phase has negative (positive) pressure anomaly over the Arctic, with the opposite anomaly equatorward. The daily AO Index is available at http://gcmd.nasa.gov/records/GCMD_NOAA_NWS_CPC_AO.html. Our plots show an association between years of increased precipitation extremes (1993–1994, 1996–1997, and 2000) and negative values of the AO Index (e.g., Figure 5). This behavior was especially evident in Alaska South, where a negative AO phase coincided with increase in widespread extreme precipitation events in land regions adjacent to the Gulf of Alaska. We find a moderate correlation of 0.62 at a statistical significance of 95%.

Matsuo and Heki [2012] found that a negative AO phase produced increased surface air temperatures and precipitation poleward of 45° in North America. *L'Heureux et al.* [2010] found similar behavior across the Arctic

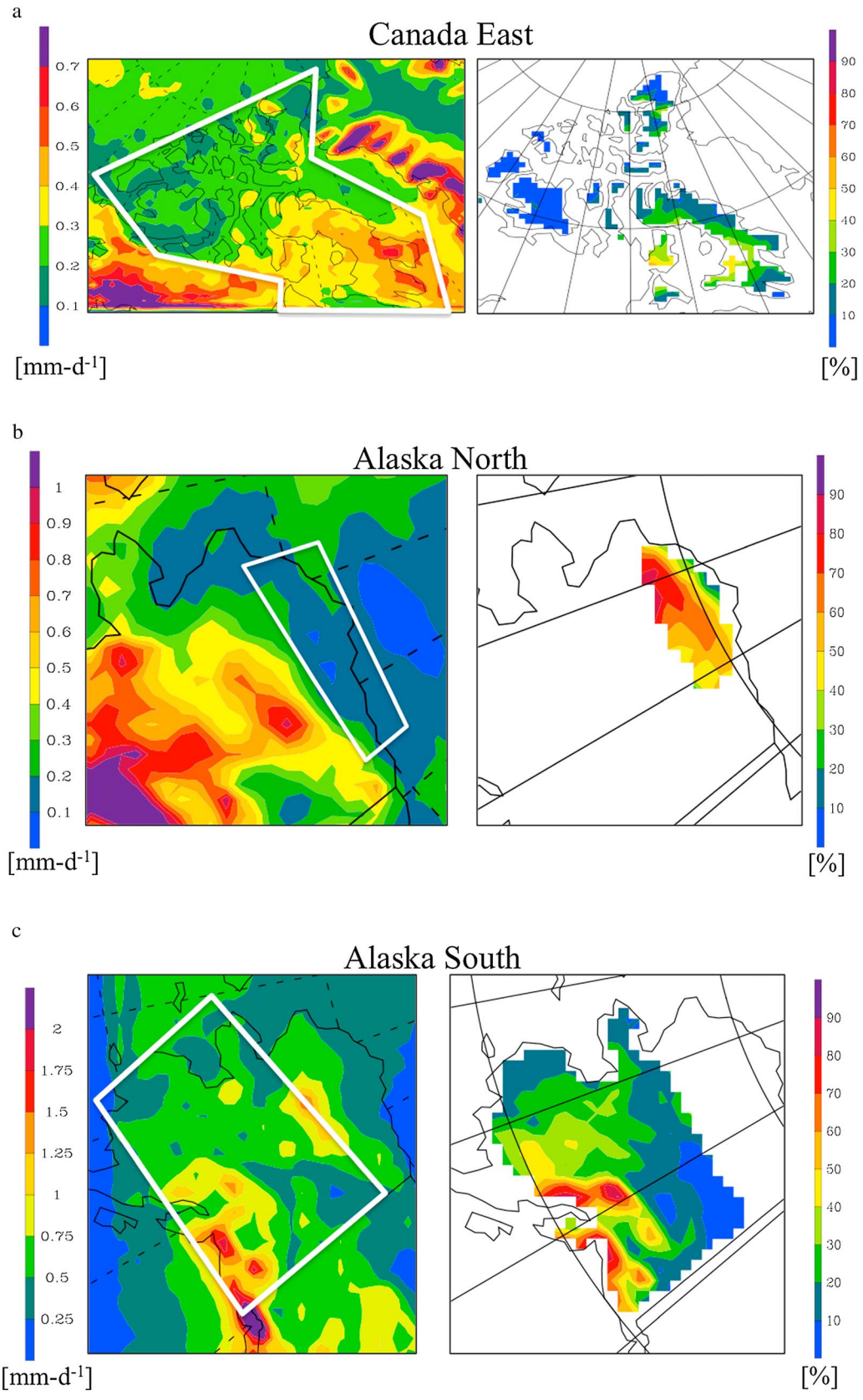

Figure 6. (left column) Composite simulated summer extreme precipitation (mm d^{-1}) for the outlined analysis region and (right column) the occurrence (%) at each grid point of spatially widespread extreme events for (a) Canada East, (b) Alaska North, and (c) Alaska South.

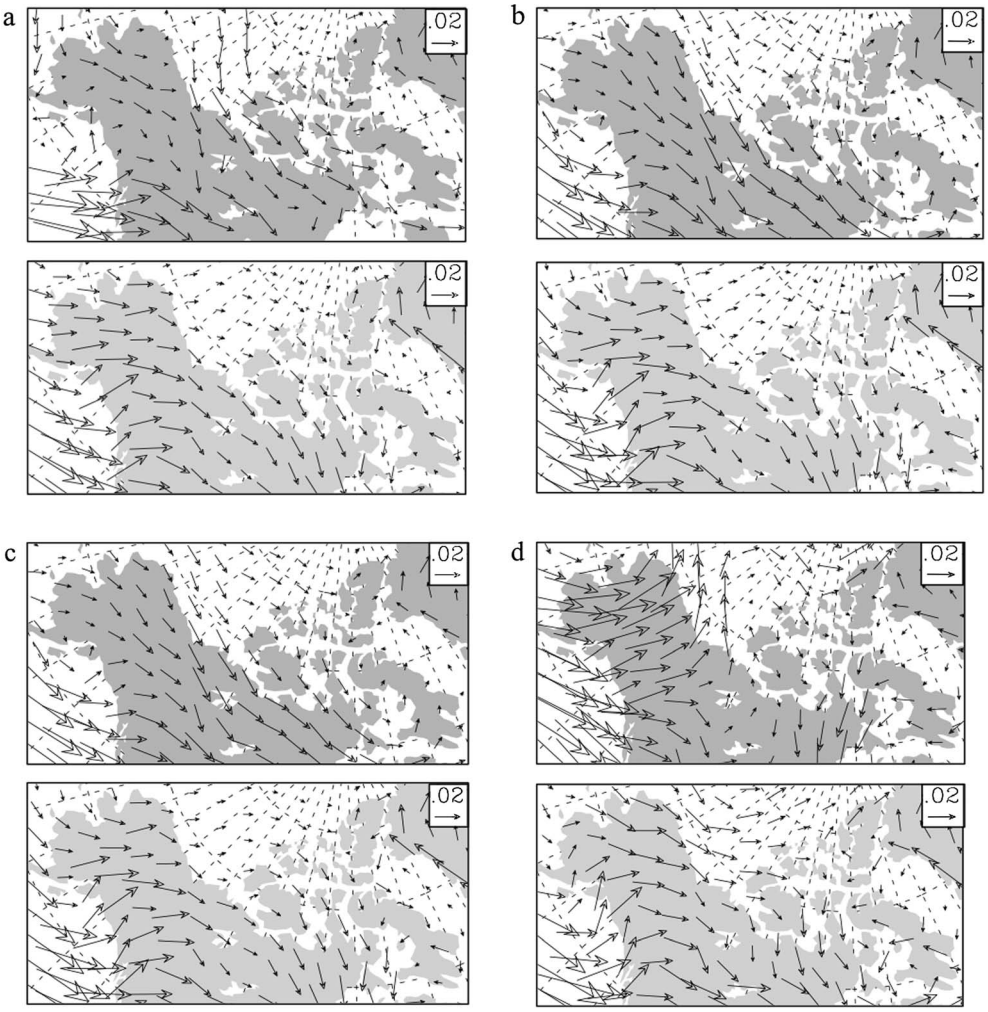

Figure 7. (a) Vertically integrated moisture flux vectors (kg kg^{-1} m s^{-1}) during extreme event days from (top) ERA-Interim and (bottom) Pan-Arctic WRF for Canada East. (b) Vertically integrated moisture flux vectors (kg kg^{-1} m s^{-1}) during extreme event days from (top) ERA-Interim and (bottom) Pan-Arctic WRF for Canada West. (c) Vertically integrated moisture flux vectors (kg kg^{-1} m s^{-1}) during extreme event days from (top) ERA-Interim and (bottom) Pan-Arctic WRF for Alaska North. (d) Vertically integrated moisture flux vectors (kg kg^{-1} m s^{-1}) during extreme event days from (top) ERA-Interim and (bottom) Pan-Arctic WRF for Alaska South.

during the negative phase. We will see later that the locations of the most frequent widespread extreme events are collocated with higher daily precipitation rates near the Gulf of Alaska. The AO pattern may also explain the close connection between ensemble members and NCDC observations during the years with very many or very few widespread extremes, suggesting the model is capturing important aspects of the Arctic Oscillation behavior.

4.4. Spatial Extent of Widespread Extreme Precipitation Events

In Figure 6, we plot composites of precipitation of days with widespread extreme events for three of our regions: Canada East, Alaska North, and Alaska South. We analyze Western Canadian region separately as we shall see that it has substantial convective precipitation during extreme events, whereas the others do not. We discuss Canada West convection in section 4.6. In Figure 6, we also have plotted the frequency of occurrence of precipitation exceeding the 99th percentile during widespread extreme events on a grid point-by-grid point basis. This plot shows the favored locations for these events in an analysis region. With this information, we then can examine surface and atmospheric fields in specific parts of the analysis region for dominant physical processes.

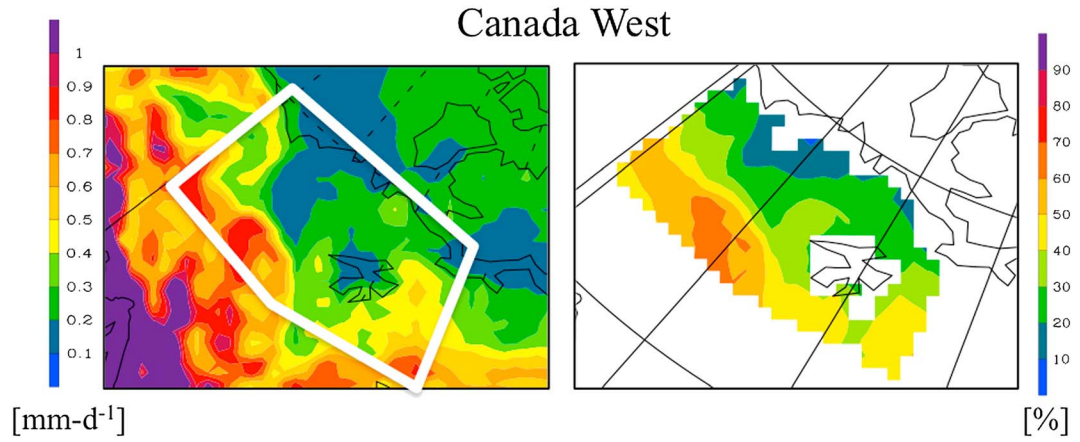

Figure 8. (left) Composite simulated summer extreme precipitation (mm d^{-1}) and (right) occurrence (%) at each grid point of spatially widespread extreme events.

Figure 6a shows that while higher overall precipitation fell on the eastern side of Baffin Island in the Eastern Canadian analysis region, the concentration of widespread extremes occurred on the western side. Alaska North exhibited somewhat different behavior in that the highest daily values of extreme precipitation were collocated with the favored location of widespread extremes (Figure 6b). Like Alaska North, Alaska South had higher overall precipitation in regions favoring widespread events, such as the Alaska Range and coastal mountains adjacent to Prince William Sound (Figure 6c). Note that the locations of highest frequency of extreme events are not necessarily also the same locations receiving the largest amounts of extreme precipitation, indicating that precipitation amounts are also influenced by factors other than frequency of events such as locations of strong orographic uplift.

4.5. Low-Level Moisture Convergence

Extreme precipitation events may be located in regions in which there is convergence of low-level moisture. Here, we have calculated the vertically integrated moisture flux vector for our analysis regions, shown in Figure 7. In each region, we find a consistent feature in that onshore flow from adjacent ocean bodies is transporting moisture inland. Moreover, flux vectors place the strongest implied moisture convergence within regional locations favored for widespread extremes. With the exception of Canada West (Figure 8), where convective processes are important, flow into the analysis regions appears to be impeded by higher topographical features; this suggests that the Alaska North, Alaska South, and Canada East regions are experiencing extreme precipitation induced by orography.

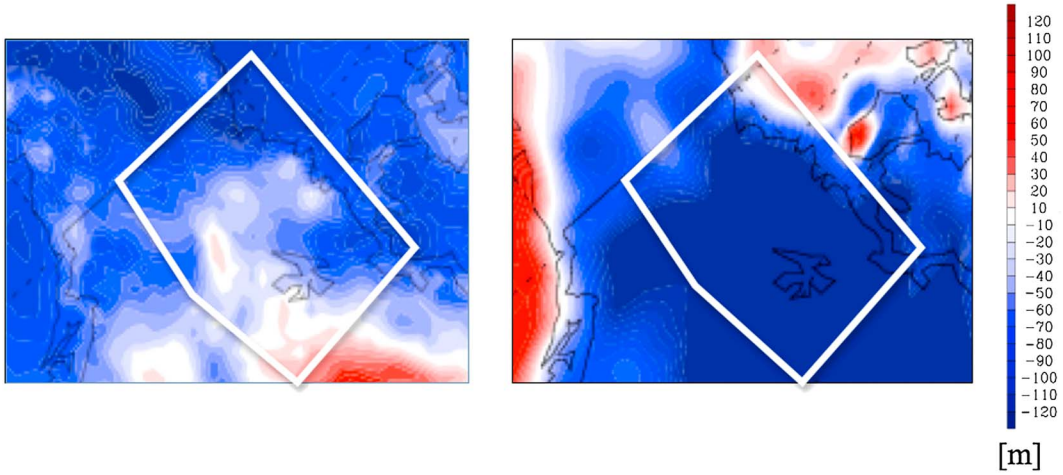

Figure 9. Composited lifting condensation level anomaly (m) (left) ERA-Interim and (right) Pan-Arctic WRF for Canada West.

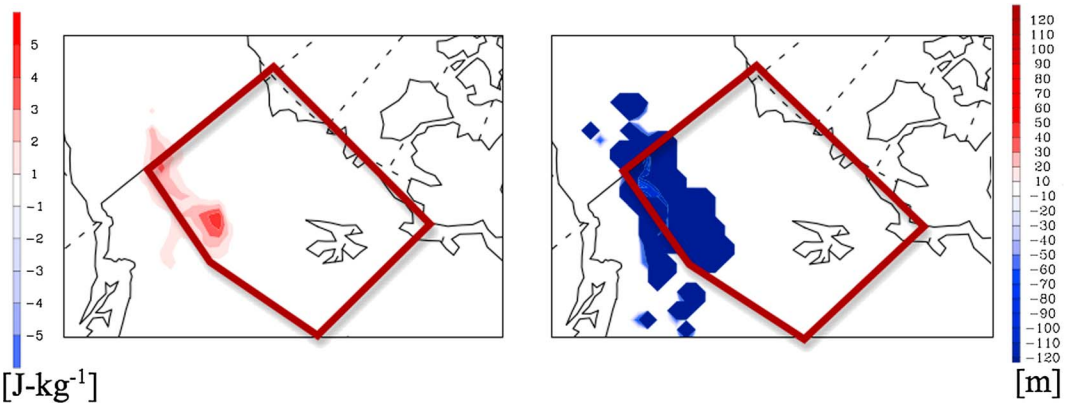

Figure 10. (left) Composited convective available potential energy anomaly (J kg^{-1}) and (right) level of free convection anomaly (m) from PAW for Canada West.

4.6. Canada West: Convective Contribution

To understand better the possible contribution by convection to widespread extreme events, we present for Canada West events composites of various convective diagnostics: the lifting condensation level (LCL), the level of free convection (LFC), and convective available potential energy (CAPE). These fields help us determine whether or not conditions are favorable for convection within the analysis region. The LCL gives the level at which a mechanically lifted surface air parcel reaches condensation. A finite LFC indicates a level where surface air parcels have positive buoyancy, thus indicating a potential convective instability. CAPE indicates the amount of buoyant energy a surface air parcel can have. Lower LCL and LFC heights, in conjunction with larger CAPE, indicate conditions more conducive for convection.

Figure 9 shows Canada West LCL anomalies for the EI and PAW. Both the reanalysis and simulated anomalies have negative values over large parts of the Canada West region. While lower LCL anomalies appeared in other regions during their widespread extreme events (not shown), LFC and CAPE values consistent with convection appeared only in Canada West (Figure 10). For this region, we found that the simulated convective contribution on widespread extreme days was nearly 60%. Moreover, the region of anomalously higher convection was collocated with the largest occurrence of widespread extreme precipitation. Finally, the most intense daily average values for extreme event days were also in the same location.

5. Conclusions

In this paper, we have analyzed a 19 year CORDEX Arctic simulation produced by a polar-modified version of the WRF model, with a goal of delineating its capabilities for producing extreme daily precipitation in summer months. The simulation was created using a six-member ensemble, forced with the ERA-Interim reanalysis and sea ice concentration from the National Snow and Ice Data Center. We discarded the first 3 years for model spin-up and analyzed output for a summer season (July-August-September) based on the sea ice cycle.

We used the 99th percentile as our definition of an extreme precipitation event. We further restricted our analysis to widespread events in which 25 or more grid points had an extreme precipitation on the same day. We defined four analysis regions over North America to determine whether the temporal and spatial distribution of extreme events varied as a function of geography and proximity to ocean bodies. We also used days of widespread extreme precipitation to create seasonal composite fields for each analysis region. Analysis of these composites along with the deviation from climatology (anomaly plots) allowed us to develop an understanding of the physical mechanisms and associated circulations responsible for producing extreme precipitation. For comparison and validation, we used the same analysis procedure on EI reanalysis output and NCDC station observations. Composites of observed surface and atmospheric fields allowed us to determine how well the simulated circulation features were consistent with real world processes producing extreme precipitation events. To establish the model's simulation credibility, we showed that the model and observations were in general agreement using seasonally averaged plots of surface and atmospheric fields.

Using frequency versus intensity histograms, we showed that the Pan-Arctic WRF consistently underestimates extreme precipitation amounts compared to the NCDC station observation. We did find that simulation and observations come into agreement at the lower end of the intensity spectrum, suggesting that the model is reproducing lower intensity events well. Despite this shortcoming, the PAW spatial scales for widespread extreme events are roughly equivalent to the observed scales.

The interannual variability of widespread extremes showed similarity to the observed variability. In general, years with the highest and lowest occurrences of observed extreme events were simulated well by the model. However, the spread among the PAW ensemble members tended to be more variable during the interim periods. These results suggest that the occurrence of extremes is partly a function of model internal variability. Agreement among ensemble members during favored years suggests a controlling factor imposed on the simulation, with the Arctic Oscillation showing some correlation with the interannual variability of widespread extreme events.

In order to locate regions within our analysis boxes where widespread extremes were more likely to occur, we calculated a grid point-by-grid point occurrence frequency. Along with the frequency, we also produced plots of daily average precipitation during extreme event days. Analysis of these plots allowed us to focus on locations that were responsible for the greatest occurrences of widespread events.

We used composites of diagnostic fields to diagnose the behavior of the atmosphere during widespread extreme precipitation events in both simulations and observations. Using composites of convection diagnostics, we found that the Canada West analysis region had a significant contribution to widespread extreme events from atmospheric convection. We performed additional analysis on the convective contribution to total extreme precipitation amounts in this region. Additionally, the highest intensity extreme daily precipitation fell in the spatial location collocated with the highest occurrence of widespread extremes. These results indicate that atmospheric convection is the primary mechanism for widespread extreme precipitation events in Western Canada during summer. The remaining analysis regions did not exhibit a significant convective contribution to extreme precipitation events.

Composite plots of surface and upper level fields for widespread events in each region showed that the large-scale circulation when extreme events occurred was similar for each region. We also found low-level flow into each region from adjacent ocean bodies was a common factor on days of widespread extreme events. Moreover, convergence in the moisture flux field gave conditions conducive for precipitation in the locations of widespread extreme events.

With the exception of Canada East, the location of highest average precipitation was always found in the region favored for widespread extreme events. Moreover, these regions were located over higher topography and thus indicated a significant orographic contribution to the extreme events. In Canada East, we found the highest average precipitation over eastern Baffin Island. The most favored region of widespread extremes, however, was found over western Baffin Island and the Melville Peninsula. Even though these regions were not collocated, orographic precipitation still appeared to be the dominant process for widespread extreme events.

Even though PAW simulated fewer high-intensity precipitation events than seen in the observations, the composite results showed that the model is reproducing well the atmospheric features conducive to the events. The composite circulations for widespread extreme events in each season examined were generally the same for each analysis region; the same general circulation pattern produces extremes in multiple regions. Coupled with the observed precipitation and the reanalysis, the model output has given us insight into the nature of precipitation extremes in these regions, highlighting the importance of moisture fetch off the adjacent oceans and topographic uplift for producing extreme precipitation. In addition, for the Western Canada region, the model's distinction between convective and nonconvective precipitation helped guide the analysis and showed the convective contribution to extreme precipitation, which would not be easily discerned in observations. Overall, the model appears to produce the physical behavior (specifically, the moisture transport) leading to extreme daily precipitation well enough that it can be used for analysis of changes in conditions yielding extreme events in future climate.

Acknowledgments

This research was supported by U.S. Department of Energy grant DEFG0207ER64463 and National Science Foundation grant ARC1023369. Computer support was provided by the University of Alaska Arctic Region Supercomputing Center (ARSC). The authors thank three anonymous reviewers for their comments, which helped improve this manuscript.

References

Barry, R. G., and M. C. Serreze (2000), Atmospheric components of the Arctic Ocean freshwater balance and their interannual variability, in *The Freshwater Budget of the Arctic Ocean*, edited by E. L. Lewis et al., pp. 45–56, Springer, New York.

Cassano, J. J., P. Uotila, A. H. Lynch, and E. N. Cassano (2007), Predicted changes in synoptic forcing of net precipitation in large Arctic river basins during the 21st century, *J. Geophys. Res.*, *112*, G04S49, doi:10.1029/2006JG000332.

Cassano, J. J., M. E. Higgins, and M. W. Seefeldt (2011), Performance of the Weather Research and Forecasting Model for month-long Pan-Arctic simulations, *Mon. Weather Rev.*, *139*, 3469–3488, doi:10.1175/MWR-D-10-05065.1.
Chen, F., and J. Dudhia (2001), Coupling an advanced land-surface/hydrology model with the Penn State/NCAR MM5 modeling system. Part I: Model description and implementation, *Mon. Weather Rev.*, *129*, 569–585.
Collins W. D., et al. (2004), Description of the NCAR Community Atmosphere Model (CAM 3.0), *Tech. Rep. NCAR/TN-464+STR*, 171 pp., Natl. Cent. for Atmos. Res., Boulder, Colo.
Comiso, J. (1999), Updated (2008), Bootstrap sea ice concentrations from NIMBUS-7 SMMR and DMSP SSM/I, 1989-2007, Boulder, Colorado U.S.A., National Snow and Ice Data Center, Digital media.
Dee, D. P., et al. (2011), The ERA Interim reanalysis: Configuration and performance of the data assimilation system, *Q. J. R. Meteorol. Soc.*, *137*, 553–597, doi:10.1002/qj.828/.
Dethloff, K., A. Rinke, R. Lehmann, J. H. Christensen, M. Botzet, and B. Machenhauer (1996), Regional climate model of the Arctic atmosphere, *J. Geophys. Res.*, *101*, 23,401–23,422.
Fisel, B. J., W. J. Gutowski Jr., J. M. Hobbs, and J. J. Cassano (2011), Multiregime states of Arctic atmospheric circulation, *J. Geophys. Res.*, *116*, D20122, doi:10.1029/2011JD015790.
Ghatak, D., and J. Miller (2013), Implications for Arctic amplification of changes in the strength of the water vapor feedback, *J. Geophys. Res. Atmos.*, *118*, 7569–7578, doi:10.1002/jgrd.50578.
Giorgi, F., C. Jones, and G. Asrar (2009), Addressing climate information needs at the regional level: The CORDEX framework, *World Meteorol. Organiz. (WMO) Bull.*, *58*, 175–183.
Glisan, J. M., W. J. Gutowski, J. J. Cassano, and M. E. Higgins (2013), Effects of spectral nudging in WRF on Arctic temperature and precipitation simulations, *J. Clim.*, *26*, 3985–3999, doi:10.1175/JCLI-D-12-00318.1.
Grell, G. A., and D. Devenyi (2002), A generalized approach to parameterizing convection combining ensemble and data assimilation techniques, *Geophys. Res. Lett.*, *29*(14), 1693, doi:10.1029/2002GL015311.
Gutowski, W. J., K. A. Kozak, R. W. Arritt, J. H. Christensen, J. Patton, and E. S. Takle (2007), A possible constraint on regional precipitation intensity changes under global warming, *J. Hydrometeorol.*, *8*, 1382–1396, doi:10.1175/2007JHM817.1.
Hines, K. M., D. H. Bromwich, L.-S. Bai, M. Barlage, and A. G. Slater (2011), Development and testing of polar WRF. Part III: Arctic Land*, *J. Clim.*, *24*, 26–48, doi:10.1175/2010JCLI3460.1.
IPCC (2007), *Climate Change 2007: The Physical Science Basis. Contribution of Working Group I to the Fourth Assessment Report of the Intergovernmental Panel on Climate Change*, pp. 996, Cambridge Univ. Press, New York.
Janjić, Z. I. (1990), The step-mountain coordinate: Physical package, *Mon. Weather Rev.*, *118*, 1429–1443.
Janjić, Z. I. (1996), The surface layer in the NCEP Eta Model, in *Preprints, 11th Conf. on Numerical Weather Prediction*, pp. 354–355, Am. Meteorol. Soc, Norfolk, VA.
Janjić, Z. I. (2002), Nonsingular implementation of the Mellor–Yamada level 2.5 scheme in the NCEP Meso model, NCEP Office Note 437, 61 pp.
Kunkel, K. E. (2003), North American trends in extreme precipitation, *Nat. Hazards*, *29*, 291–305.
L'Heureux, M., A. Butler, A. Jha, A. Kumar, and W. Wang (2010), Unusual extremes in the negative phase of the Arctic Oscillation during 2009, *Geophys. Res. Lett.*, *37*, L10704, doi:10.1029/2010GL043338.
Matsuo, K., and K. Heki (2012), Anomalous precipitation signatures of the Arctic oscillation in the time-variable gravity field by GRACE, *Geophys. J. Int.*, *130*, 1495–1506, doi:10.1111/j.1365-246X.2012.05588.x.
Matthes, H., A. Rinke, and K. Dethloff (2010), Variability of extreme temperature in the Arctic—Observation and RCM, *Atmos. Sci. J.*, *4*, 126–136.
Mlawer, E. J., S. J. Taubman, P. D. Brown, M. J. Iacono, and S. A. Clough (1997), Radiative transfer for inhomogeneous atmospheres: RRTM, a validated correlated-k model for the longwave, *J. Geophys. Res.*, *102*, 16,663–16,682, doi:10.1029/1997JD00237.
Monin, A. S., and A. M. Obukhov (1954), Basic laws of turbulent mixing in the surface layer of the atmosphere, *Contrib. Geophys. Inst. Acad. Sci.*, *151*, 163–187.
National Climatic Data Center (2011), NESDIS, NOAA, U.S. Department of Commerce: Global Surface Summary of the Day—GSOD, [Internet]. National Climatic Data Center, Asheville, NC. [Available at http://www.ncdc.noaa.gov/cgi-bin/res40.pl?page=gsod.html.]
Oort, A. H. (1983), *Atmospheric Circulation Statistics*, 173 pp., NOAA Prof. Paper 5, U.S. Dept. of Commerce, Rockville, U.S.
Schindler, D. W., and J. P. Smol (2006), Cumulative effects on climate warming and other human activities on freshwater Arctic and subarctic North America, *Ambio*, *35*(4), 160–168.
Serreze, M. C., A. P. Barrett, J. C. Stroeve, D. N. Kindig, and M. M. Holland (2009), The emergence of surface-based Arctic amplification, *Cryosphere*, *3*, 11–19.
Serreze, M. C., J. A. Maslanik, and J. Key (1997), Atmospheric and sea ice characteristics of the Arctic Ocean and the SHEBA field region of the Beaufort Sea, NSIDC, Special Report 4, Boulder, CO.
Skamarock, W. C., J. B. Klemp, J. Dudhia, D. O. Gill, D. M. Barker, M. Duda, X.-Y. Huang, and J. G. Powers (2008), A description of the Advanced Research WRF version 3, *NCAR Tech. Note NCAR/TN-475+STR*, 113 pp., Natl. Cent. for Atmos. Res., Boulder, Colo.
Tao, W. K., and J. Simpson (1993), The Goddard cumulus ensemble model. Part I: Model description, *Terr. Atmos. Oceanic Sci.*, *4*, 19–54.
Taschetto, A. S., and M. H. England (2008), Estimating ensemble size requirements of AGCM simulations, *Meteorol. Atmos. Phys.*, *100*, doi:10.1007/s00703-008-0293-8.
Tebaldi, C., K. Hayhoe, J. M. Arblaster, and G. A. Meehl (2006), Going to the extremes: An intercomparison of model-simulated historical and future changes in extreme events, *Clim. Change*, *79*, 185–211, doi:10.1007/s10584-006-9051-4.
Thompson, D. W. J., and J. M. Wallace (1998), The Arctic oscillation signature in the wintertime geopotential height and temperature fields, *Geophys. Res. Lett.*, *25*, 1297–1300.
Thompson, D. W. J., and J. M. Wallace (2001), Regional climate impacts of the Northern Hemisphere annular mode, *Science*, *293*, 85–89.
Wei, H., W. J. Gutowski Jr., C. J. Vörösmarty, and B. M. Fekete (2002), Calibration and validation of a regional climate model for Pan-Arctic hydrologic simulation, *J. Clim.*, *15*, 3222–3236.
Wilks, D. S. (1995), *Statistical Methods in the Atmospheric Sciences: An Introduction*, pp. 467, Academic Press, Amsterdam, The Netherlands.
Zhang, X., W. D. Hogg, and É. Mekis (2001), Spatial and temporal characteristics of heavy precipitation events over Canada, *J. Clim.*, *14*, 1923–1936, doi:10.1175/1520-0442(2001)014<1923:SATCOH>2.0.CO.